PFEM formulation for thermo-coupled FSI analysis. Application to nuclear core melt accident.

Alessandro Franci [*1,2], Eugenio Oñate[1,2], Josep Maria Carbonell[1,2], and Michele Chiumenti[1,2]

[1] International Center for Numerical Methods in Engineering (CIMNE)
[2]Universitat Politècnica de Catalunya (UPC)
Gran Capitán s/n, Campus Norte UPC, 08034 Barcelona, Spain

July 29, 2017

Abstract

The aim of this paper is to present a Lagrangian formulation for thermo-coupled fluid-structure interaction (FSI) problems and to show its applicability to the simulation of hypothetical scenarios of a nuclear core melt accident. During this emergency situation, an extremely hot and radioactive lava-like material, the corium, is generated by the melting of the fuel assembly. The corium may induce collapse of the nuclear reactor devices and, in the worst case, breach the reactor containment and escape into the environment. This work shows the capabilities of the proposed formulation to reproduce the structural failure mechanisms induced by the corium that may occur during a meltdown scenario. For this purpose, a monolithic method for FSI problems, the so-called Unified formulation, is here enhanced in order to account for the thermal field and to model phase change phenomena with the Particle Finite Element Method (PFEM). Several numerical examples are presented. First, the convergence of the thermo-coupled method and phase change algorithm is shown for two academic problems. Then, two complex simulations of hypothetical nuclear meltdown situations are studied in 2D as in 3D.

*email: falessandro@cimne.upc.edu

1 Introduction

In this work, a Lagrangian formulation for phase change problems is proposed and its potential for simulating hypothetical scenarios of a nuclear core melt accident, also called nuclear severe accident (NSA), is shown. In situations in which the emergency core cooling system of the nuclear reactor is not operative, the overheating generated by the decay heat of the fission products contained in the fuel rods, may induce the core melting and the formation of a dangerous substance called *corium*. This material is extremely hot, toxic and radioactive and it may induce the collapse of those nuclear reactor devices. The seriousness of this scenario is related to the possibility that the corium breaches all containment and escapes into the environment, producing radioactive contamination.

There is a high interest on improving the actual forecasting capabilities for the NSA and to determine the debris distribution and relocation within the reactor.

From the numerical point of view, the nuclear core melt accident simulation is extremely challenging. The study requires a numerical tool able to deal with free-surface fluids interacting with structures that undergo large displacements, thermo-plastic deformations, and phase change. Furthermore, also chemical and radioactive reactions play a relevant role and affect the temperature and behavior of corium. Finally, the geometries involved in a NSA are complex and the analyses should generally be carried out in three dimensions (3D).

The complexity of this scenario explains why numerical methods have not been largely used for the NSA simulation and, when employed, strong simplifications and hypotheses have been assumed.

Recently, some interesting attempts to simulate numerically specific NSA scenarios have been done [11, 47, 38, 48, 70]. In [71] the relocation of molten materials in nuclear reactors was modeled using a thermo-coupled Volume of Fluid (VOF) method [30], while in [10] the flow and solidification of molten core debris was studied with the Moving Particle Semi-implicit (MPS) method [41]. The same method was used in [9] and in [44, 69] for modeling the effect of corium on the fuel support piece and the concrete basement, respectively. There also exist computational frameworks entirely devoted to severe accident simulation as MAAP [66], SAMPSON [65, 59], and MELCOR [42, 43].

Most of the mentioned works focus on the fluid part analysis, while the structural components of the nuclear reactor are treated with simplified models, generally as rigid bodies, unable to reproduce their thermo-plastic deformation.

Nevertheless, the radioactive debris relocation occurring during a nuclear meltdown is highly affected by the collapse mechanisms of the nuclear reactor solid components. Hence, an accurate simulation of the structural failure is of key importance in order to have a reliable NSA prediction.

This work focuses on this specific aspect of the NSA. In particular, it aims to show that the proposed method has the capability to reproduce not only the corium flow and relocation within the reactor pressure vessel but also the structural failure of the nuclear reactor internals. On the other hand, other phenomena occurring during a NSA, as the chemical and radioactive reactions

or the corium re-solidification, are considered out of the scope of this work.

The interaction between the corium and the nuclear reactor devices is handled by the so-called Unified formulation for fluid-structure interaction (FSI) problems proposed and validated in [26, 34]. The unified solution of fluid and solid mechanics allows for a monolithic computation of the FSI ensuring a strong coupling. Both fluids and solids are solved using a velocity-pressure implicit scheme. The method employs the Particle Finite Element Method (PFEM) [35, 36, 53] for the free-surface fluid dynamics and a hypoelasto-plastic Finite Element Method (FEM) [27] for solids.

The Unified formulation is enhanced in this work in order to account for thermal effects and phase change phenomena. The unified treatment of fluid and solid mechanics together with the versatility of the PFEM are particularly useful for modeling the transition from the solid to the fluid phase and vice versa.

The accuracy and convergent behavior of the thermo-coupled method including the phase change phenomena are analyzed by solving two academic problems.

Then, the numerical simulation of two hypothetical scenarios of a nuclear meltdown is presented with the aim of showing the potential of the numerical method to simulate the different phases of a NSA scenario, from the melting of the fuel bars to the collapse of the nuclear reactor devices. In both analyses, a volume of corium is made to interact with specific components of the nuclear reactor, as the core support plate and the fuel support clasp, and the collapse mechanisms of these structures are studied. In order to reduce the complexity and computational time of these simulations, some simplifying hypotheses have been assumed. The implications of these assumptions are discussed.

The paper is organized as follows. In Section 2, the governing equations together with the constitutive laws for the structure and the corium are stated. In Section 3, the algorithm for solving the thermo-mechanical problem is detailed. In Section 4, the essential features of the PFEM approach for thermal coupled FSI problems are explained and the strategy for modeling phase change phenomena is described. Then, two academic thermo-coupled FSI problems are proposed to test the convergence of the proposed method. Finally, in Section 6, the numerical simulation of two hypothetical scenarios of a nuclear core melt accident are shown and discussed.

2 Governing equations

The governing equations of the problem are the balance of linear momentum, the mass conservation and the energy balance equations. All these are solved in an Updated Lagrangian framework.

For a dynamic problem, the balance of linear momentum equation is

$$\rho \dot{\boldsymbol{v}} - \bigtriangledown \cdot \boldsymbol{\sigma} - \boldsymbol{b} = 0 \qquad in\ \Omega \times (0,t) \tag{1}$$

where ρ is the density of the material, $\boldsymbol{v}$ is the velocity vector, $\boldsymbol{\sigma}$ is the Cauchy

stress tensor, $\boldsymbol{b}$ is the body force per unit of volume, Ω is the updated, or deformed, computational domain, and t is the time.

The mass balance, or continuity equation, is solved in the quasi-incompressible form [34, 56] as

$$\frac{1}{\kappa}\dot{p} - \bigtriangledown \cdot \boldsymbol{v} + \alpha\dot{T} = 0 \qquad in\ \Omega \times (0,t) \tag{2}$$

where p is the pressure, κ is the bulk modulus of the material, α is the thermal expansion coefficient and T is the temperature.

Eq.(2) holds for incompressible, quasi-incompressible and compressible bodies, depending on the value of the bulk modulus κ. Considering isothermal conditions, for $\kappa \to \infty$ the fully-incompressible form of the continuity equation ($\bigtriangledown \cdot v = 0$) is recovered.

When dealing with the heat transfer analysis, both solidification and cooling phases are controlled by the balance of energy equation. This governing equation can be stated as

$$\dot{H} = -\nabla \cdot \mathbf{q} + R + \dot{D}_{mech} \tag{3}$$

where $\dot{H}$ is the enthalpy rate (per unit of volume), $\mathbf{q}$ is the heat flux, while R and $\dot{D}_{mech}$ represent the heat source (per unit of volume) and the thermo-mechanical dissipation rate (per unit of volume), respectively.

On the one hand, the thermo-mechanical dissipation is relevant when studying forging or extrusion processes, on the other hand its contribution can be neglected if compared to the latent heat released during melting processes (see [19] and [8] for application to metal casting processes or [14], [13] and [15] in electron beam welding and additive manufacturing analysis).

The enthalpy $H\left(T, f_L\right)$ is a state variable defined as a function of the temperature, T, and the liquid fraction, f_L. Hence, the enthalpy rate in Eq.(3) results in

$$\dot{H}\left(T, f_L\right) = \frac{\partial H}{\partial T}\dot{T} + \frac{\partial H}{\partial f_L}\dot{f}_L = C\dot{T} + L\dot{f}_L \tag{4}$$

where $C\left(T\right) = \frac{\partial H}{\partial T}$ is the (temperature dependent) heat capacity and $L = \frac{\partial H}{\partial f_L}$ is the latent heat released during the phase-change process.

The heat capacity is usually defined as $C = \rho c_v$, where c_v is the specific heat.

During the phase transformation the material volume, Ω, can be split into liquid and solid phases as: $\Omega = \Omega_L + \Omega_S$. The liquid and solid fractions are defined as $f_L = \frac{\Omega_L}{\Omega}$ and $f_S = \frac{\Omega_S}{\Omega}$, respectively, so that $f_L + f_S = 1$. The evolution of the liquid fraction $\dot{f_L}$ or, alternatively, $\dot{f_S} = -\dot{f_L}$ defines the phase change, that is, how the latent heat is absorbed or released during the transformation.

The heat flux $\mathbf{q}$, is computed as a function of the temperature gradient through the law of Fourier as

$$\mathbf{q} = -\lambda\nabla T \tag{5}$$

where $\lambda(T)$ is the (temperature dependent) thermal conductivity.

Neglecting the contribution of the mechanical dissipation and using Eq.(4), Eq.(3) transforms into

$$\rho c_v \dot{T} + L\dot{f}_L = \bigtriangledown \cdot (\lambda \bigtriangledown T) + R \tag{6}$$

The problem needs to be complemented by appropriate initial and boundary conditions.

2.1 Constitutive model for melted metals and corium

The corium has been modeled using a constitutive law for melted metals, assuming a predominance of metals in its composition.

Melting metals are characterized by such large strains so that the elastic deformations can be considered negligible compared to the visco-plastic strains [75, 13]. Hence, the stresses can be computed as function of the strain rates as

$$\boldsymbol{\sigma} = f(\boldsymbol{d}) \tag{7}$$

where $\boldsymbol{d}$ is the deformation rate tensor which is computed from the velocities as

$$\boldsymbol{d} = \frac{1}{2}\left(\bigtriangledown \boldsymbol{v} + (\bigtriangledown \boldsymbol{v})^T\right) \tag{8}$$

The von Mises flow rule is the most common one in metal plasticity [3]. It is well known that this approach does not allow volume changes [76, 6]. Hence, in order to avoid locking phenomena [50, 46], the Cauchy stress tensor is split into volumetric and deviatoric parts as follows

$$\boldsymbol{\sigma} = \boldsymbol{\sigma'} - p\boldsymbol{I} \tag{9}$$

where $\boldsymbol{\sigma'}$ is the deviatoric part of the Cauchy stress tensor and $\boldsymbol{I}$ is the second order identity tensor.

The pressure is computed from Eq.(2) while the deviatoric Cauchy stresses is related to the deviatoric strain rates as

$$\boldsymbol{\sigma'} = 2\tilde{\mu}_{eff}\boldsymbol{d'} \tag{10}$$

where $\mu_{eff}(\sigma, \boldsymbol{d}, T)$ is the effective viscosity that may depend on stresses, strains and temperature, and $\boldsymbol{d'}$ is the deviatoric part of the deformation rate tensor.

Varying the constitutive models used for the effective viscosity, the above framework is suitable for both Newtonian and non-Newtonian fluid models, as well as for rigid-visco-plastic formulations [12].

Defining the effective viscosity according to the standard Norton-Hoff visco-plastic model [51, 31], both Newtonian and non-Newtonian models can be recovered [12]. According to this visco-plastic model, the effective viscosity is defined as

$$\mu_{eff} = \mu\left(\sqrt{3}\bar{\epsilon}\right)^{m-1} \tag{11}$$

where μ is the dynamic viscosity, $\bar{\epsilon} = \sqrt{\frac{2}{3}\boldsymbol{d} : \boldsymbol{d}}$ is the deviatoric strain invariant and $0 \leq m \leq 1$ is the rate-sensitivity parameter. Note that both values may depend on the temperature.

For $m \neq 1$, a non-Newtonian model is obtained, while for $m = 1$ the Newtonian law is recovered.

A specific type of non-Newtonian law is the so-called *flow approach* [28, 73]. This technique has been extensively applied for the simulation of hot metals undergoing manufacturing processes, such as extrusion or hot rolling [74, 75].

On the other hand, in casting processes Newtonian models are generally employed [16, 17].

Newtonian viscous laws are also the most common choice for modeling the corium in NSA simulations [10, 9, 71]. Therefore, this is the model chosen for the numerical examples presented in this work.

Considering $m = 1$ and substituting Eq.(11) into Eq.(9), the standard Newtonian constitutive expression for the deviatoric stresses is recovered as

$$\boldsymbol{\sigma'} = 2\mu\boldsymbol{d'} \tag{12}$$

2.2 Constitutive model for solid structures

A thermo-hypoelasto-plastic model is used to describe the structural behavior of the solid elements. The model is derived from the hypoelastic-plastic formulation presented and validated in [27].

Hypoelastic laws lay on a direct relation between the stress rate and deformation rates [64], which can be written in a general form as

$$\boldsymbol{\sigma}^{\triangledown} = g(\boldsymbol{d}) \tag{13}$$

where $\boldsymbol{\sigma}^{\triangledown}$ is the Cauchy stress rate tensor.

The dependency of the stress measure on the deformation rate facilitates the coupling of hypoelastic models with velocity-based schemes, which are typically used in fluid dynamics. Note in fact the similarity between Eq.(13) and Eq.(7) used for the fluid part computation. This feature enables the solution of FSI problems with a monolithic and well-conditioned approach and represents the main idea underlying the Unified formulation [34, 26].

Nevertheless, it is worth to highlight that hypoelasticity has some inconveniences [61, 76, 4, 37], as the lack of energy conservation in large elastic deformation processes [55], the introduction of artificial elastic dissipation [40, 63] or the spurious shear oscillations in shear dominated processes [21, 49].

Most of the drawbacks of hypoelasticity are due to the lack of an underlying elastic potential, as for hyperelasticity [62, 60]. As a consequence, hypoelastic models do not ensure a null work in a closed deformation path [55]. However, this error can be considered negligible when elastic strains are small compared to the total deformations [3]. This explains why hypoelasticity is generally used for problems dominated by plastic deformations, as manufacturing processes

[4, 29, 24], and can be considered adequate for NSA simulations where the structural components undergo large plastic deformations.

As for melted metals, the volumetric part of the stress tensor is computing using Eq.(2), while the deviatoric part is obtained by the objective time integration [3, 27] of the Jaumann measure of the Cauchy stress rate $\boldsymbol{\sigma}^{J\triangledown}$ as

$$\boldsymbol{\sigma'}^{J\triangledown} = \boldsymbol{c'}^{\sigma J} : \boldsymbol{d'}^{el} \tag{14}$$

where $\boldsymbol{c'}^{\sigma J}$ and $\boldsymbol{d'}^{el}$ are the Jaumann tangent moduli tensor and elastic deformation rate tensor, respectively.

Considering an isotropic material and assuming that the elastic volume changes g so small that the Cauchy and the Kirchhoff stress tensors are almost equivalent [4, 3], $\boldsymbol{c'}^{\sigma J}$ reads

$$\boldsymbol{c'}^{\sigma J} = 2\mu \mathbf{I'} \tag{15}$$

where μ is the shear modulus and $\mathbf{I'}$ is a fourth-oder tensor defined as $\mathrm{I}'_{ijkl} = \frac{1}{2}\left(\delta_{ik}\delta_{jl} + \delta_{il}\delta_{kj} - \frac{2}{3}\delta_{ij}\delta_{kl}\right)$, where δ_{ij} is the Kronecker delta.

Assuming the additively decomposition of the strain rates into the elastic and plastic parts [45, 39], the elastic deviatoric deformation rate tensor is computed as

$$\boldsymbol{d'}^{el} = \boldsymbol{d'} - \boldsymbol{d}^{vp} \tag{16}$$

where $\boldsymbol{d'}$ is the deviatoric part of the total deformation rate and $\boldsymbol{d}^{vp}$ is visco-plastic deformation rate tensor, deviatoric by definition.

Substituting Eqs.(16, 15) into Eq.(14) and integrating within the step $\left[{}^{n}t, {}^{n+1}t\right]$ of duration Δt, the deviatoric part of the Cauchy stress at ${}^{n+1}t$ is computed as

$${}^{n+1}\boldsymbol{\sigma'} = {}^{n}\hat{\boldsymbol{\sigma'}} + 2\Delta t\mu^{n+1}\boldsymbol{d'} - 2\Delta t\mu^{n+1}\boldsymbol{d}^{vp} \tag{17}$$

where ${}^{n}\hat{\boldsymbol{\sigma'}}$ is the deviatoric part of the Cauchy stress of the previous time step rotated in order to respect the objectivety, or frame invariance, of the scheme [3, 4, 27].

The first two terms at the right hand side of Eq.(17) represent the trial elastic prediction, while the last term is the plastic correction.

The visco-plastic response is defined by the J_2 flow model as

$$\boldsymbol{d}^{vp} = \dot{\gamma}\boldsymbol{r} \tag{18}$$

where $\dot{\gamma}$ is the plastic multiplier given by

$$\dot{\gamma} = \frac{1}{\eta}\sigma_Y(T)\left\langle \frac{\bar{\sigma} - \sigma_Y(T)}{\sigma_Y(T)} \right\rangle^m \tag{19}$$

being η is the plastic viscosity, σ_Y is the temperature-dependent yield stress, $\langle\cdot\rangle$ are the Macaulay brackets and $\bar{\sigma}$ is the effective stress computed as $\bar{\sigma} = \sqrt{\frac{3}{2}\sigma'_{ij}\sigma'_{ij}}$.

Considering an associative plastic model, the plastic flow direction, $\boldsymbol{r}$, is computed as

$$\boldsymbol{r} = \frac{3}{2\bar{\sigma}}\boldsymbol{\sigma}' \tag{20}$$

Above the melting point, the constitutive behavior is assumed to be purely visco-plastic, so that $\boldsymbol{d}' = \boldsymbol{d}^{vp}$. Furthermore, at this state, the temperature-dependent yield stress vanishes and the rate sensitive parameter is taken as $m = 1$ [13, 12, 20]. Considering this and substituting Eqs.(19) and (20) into Eq.(18), the following relation for the deviatoric deformations of melted solids is obtained

$$\boldsymbol{d}' = \boldsymbol{d}^{vp} = \frac{3}{2\eta}\boldsymbol{\sigma}' \tag{21}$$

Note that this relation is compatible with the Newtonian model (Eq.(12)). This allows for a smooth transition for the phase-change simulation, if a proper temperature-dependency of the material parameters is established.

3 Solution scheme

The numerical solution of the coupled thermo-mechanical problem (Eqs.(1, 2,6)) involves the transformation of an infinite dimensional transient system into a sequence of discrete non-linear algebraic problems. This can be achieved by means of a Galerkin finite element projection and a time-marching scheme for the advancement of the primary nodal variables, velocities, pressure and temperatures, together with a return mapping algorithm to update of the internal variables.

With regard to the time stepping scheme different strategies are possible, but they can be grouped in two categories: simultaneous (monolithic) solution and staggered (block-iterative or fractional-step) time-stepping algorithms.

In this work a weakly-coupled staggered solution has been chosen. In particular, the FSI problem (Eqs.(1, 2)) is solved assuming isothermal conditions. Then, the thermal problem (Eq.(6)) is solved in the updated and fix configuration. In Figure 1 a scheme of the algorithm is shown.

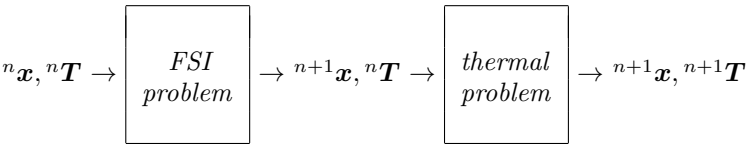

Figure 1: Staggered weakly-coupled scheme for a generic time step $({}^{n}t, {}^{n+1}t)$.

A product formula algorithm has been introduced leading to a time-integration scheme in which the two sub-problems (thermal and mechanical) are solved sequentially, within the framework of classical fractional step methods ([1, 2]).

As a result, the original coupled problem is split into two smaller and typically symmetric partitions allowing the use of any integration technique originally developed for the uncoupled sub-problems.

The final result is an accurate, efficient and robust numerical strategy, which allows the numerical simulation of large coupled thermo-mechanical problems including phase-change ([19, 8, 14]).

Both mechanical and thermal problems are solved using the FEM. The computational domain is discretized using 3-noded triangles (for 2D problems) and 4-noded tetrahedra (for 3D problems). The nodal unknowns (velocities, pressure, and temperature) are interpolated using linear shape functions. The derivation of the fully discretized and linearized form falls outside the objective of this article and it can be found in [26].

The mechanical problem is solved via the iterative partitioned Gauss-Seidel two-step scheme proposed in [26]. For each time step increment, the linear momentum equations (Eq.(1)) and the continuity equation (Eq.(2)) are solved iteratively for the increments of velocity and the pressure, respectively, until convergence is achieved.

In order to deal with the discontinuity of the pressure field at the fluid-solid contour, two different degrees of freedom for the nodal pressures are defined for all nodes at the fluid-solid interface. The continuity equation (Eq.(2)) is solved twice for these nodes, first for the structure and then for the melted material. The continuity equation is solved using the Finite Increment Calculus (FIC) stabilized approach proposed in [52], in order to circumvent the *LBB* condition [5].

Algorithm 1 describes the FSI solution for a generic time step $[{}^{n}t; {}^{n+1}t]$ of duration Δt considering the matrix form of the problem [26]. Subscripts 's' and 'f' refer to solid and fluid elements, respectively. The variables marked with a upper bar are nodal values. All the variables, vectors and matrices introduced in Algorithm 1 are listed and defined in Box 1.

After the solution of the mechanical problem, the heat transfer problem (Eq.(6)) is solved in the updated configuration.

4 PFEM for thermo-coupled FSI problems

The PFEM [68] is particularly adequate for those problems where severe changes of topology occur. This is the case of free-surface fluid dynamics [18], large-strain solid mechanics [7], FSI problems [72] and thermal coupled problems [54]. The NSA simulation belongs to this class of problems.

The essential idea of the PFEM is to follow the topology of the deformed bodies by moving the nodes of the mesh according to the equations of motion in a Lagrangian framework. This implies the regeneration of the mesh whenever it exceeds a threshold of distortion.

The remeshing strategy is one of the most characteristic features of the PFEM [33]. At each time step the good quality of the mesh is guaranteed

For a given temperature ${}^{n}T$, at each iteration i:

1. Compute the nodal velocity increments $\boldsymbol{\Delta}\bar{\boldsymbol{v}}_{s,f}$:

$\boldsymbol{K}^i \boldsymbol{\Delta}\bar{\boldsymbol{v}}_{s,f} = \boldsymbol{R}^i_{s,f}(\bar{\boldsymbol{v}}^i_{s,f}, \bar{\boldsymbol{p}}^i_{s,f})$

where: $\boldsymbol{K}^i = \boldsymbol{K}^m(\bar{\boldsymbol{x}}^i, \boldsymbol{c}^\sigma_{f,s}) + \boldsymbol{K}^g(\bar{\boldsymbol{x}}^i, \boldsymbol{\sigma}^i) + \boldsymbol{K}^\rho(\bar{\boldsymbol{x}}^i)$

2. Update nodal velocities: ${}^{n+1}\bar{\boldsymbol{v}}^{i+1}_{s,f} = {}^{n+1}\bar{\boldsymbol{v}}^{i}_{s,f} + \boldsymbol{\Delta}\bar{\boldsymbol{v}}_{s,f}$

3. Update nodal coordinates: ${}^{n+1}\bar{\boldsymbol{x}}^{i+1}_{s,f} = {}^{n+1}\bar{\boldsymbol{x}}^{i}_{s,f} + \bar{\boldsymbol{u}}_{s,f}(\boldsymbol{\Delta}\bar{\boldsymbol{v}}_{s,f})$

4. Compute fluid nodal pressures $\bar{\boldsymbol{p}}^{i+1}_f$: $\boldsymbol{H}_f \bar{\boldsymbol{p}}^{i+1}_f = \boldsymbol{F}_{pf}(\bar{\boldsymbol{v}}^{i+1}_f, \bar{\boldsymbol{p}}^{i}_f)$

where: $\boldsymbol{H}_f = \left(\frac{1}{\Delta t}\mathbf{M}_{1f} + \frac{1}{\Delta t^2}\mathbf{M}_{2f} + \mathbf{L}_f + \mathbf{M}_{bf}\right)$

and $\boldsymbol{F}_{pf} = \frac{\mathbf{M}_{1f}}{\Delta t}{}^{n}\bar{\boldsymbol{p}}_f + \frac{\mathbf{M}_{2f}}{\Delta t^2}\left({}^{n}\bar{\boldsymbol{p}}_f + {}^{n}\bar{\dot{\boldsymbol{p}}}_f \Delta t\right) + \mathbf{Q}^T\ \bar{\boldsymbol{v}}^{i+1}_f + \boldsymbol{f}_{pf}$

5. Compute solid nodal pressures $\bar{\boldsymbol{p}}^{i+1}_s$: $\frac{1}{\Delta t}\mathbf{M}_{1s}\bar{\boldsymbol{p}}^{i+1}_s = \boldsymbol{F}_{ps}(\bar{\boldsymbol{v}}^{i+1}_s, \bar{\boldsymbol{p}}^{i}_s)$

where: $\boldsymbol{F}_{ps} = \mathbf{Q}^T\ {}^{n+1}\bar{\boldsymbol{v}}^{i+1}_s + \frac{\mathbf{M}_{1s}}{\Delta t}{}^{n}\bar{\boldsymbol{p}}_s$

6. Compute fluid and solid stresses: $\boldsymbol{\sigma}^{i+1}_f,\ \boldsymbol{\sigma}^{i+1}_s$

7. Check the convergence: $\dfrac{\|\Delta\bar{\boldsymbol{v}}^{i+1}_{f,s}\|}{\|{}^{n}\bar{\boldsymbol{v}}_{s,f}\|} \leq e_v \quad \dfrac{\|\bar{\boldsymbol{p}}^{i+1}_{f,s} - \bar{\boldsymbol{p}}^{i}_{f,s}\|}{\|{}^{n}\bar{\boldsymbol{p}}_{f,s}\|} \leq e_p$

with e_v and e_p prescribed error norms for velocities and pressures.

If condition 7 is not fulfilled, return to 1 with $i \leftarrow i+1$.

Algorithm 1: Iterative solution scheme for the FSI problem [26].

through an efficient algorithm that combines the Delaunay triangulation [57, 23] and the Alpha Shape method [22].

This remeshing algorithm allows for the treatment of large deforming bodies and to face complex highly non-linear problems. However, it has associated some drawbacks that should be taken in consideration. In particular, the remeshing in the PFEM induces artificial changes of topology by adding and erasing elements during the transition from the old mesh to the new one. These modifications may induce pressure concentrations and a global volume variation. These issues have been analyzed in [25], where the convergence of the method is also shown.

In the context of FSI algorithms, the PFEM is classified as a body fitted (or conforming) strategy. In fact, at the fluid-solid interface a node to node correspondence is guaranteed. This facilitates the transfer of boundary conditions which is performed without interpolation procedures that may affect the accuracy of the FSI model.

The basic steps of the PFEM algorithm are shown in Figure 2.

$$R^i_{Ii} = \int_\Omega N_I \rho N_J d\Omega \; \bar{\dot{v}}^i_{Ji} + \int_\Omega \frac{\partial N_I}{\partial x_j} \sigma^i_{ij} d\Omega - \int_\Omega {N_I}^{n+1} b_i d\Omega - \int_{\Gamma_t} {N_I}^{n+1} t^p_i d\Gamma$$

$$\boldsymbol{K}^m_{IJ} = \int_\Omega \boldsymbol{B}^T_I \Delta t \boldsymbol{c}^\sigma_{f,s} \boldsymbol{B}_J d\Omega, \;\; \boldsymbol{K}^g_{IJ} = \boldsymbol{I} \int_\Omega \boldsymbol{\beta}^T_I \Delta t \boldsymbol{\sigma} \boldsymbol{\beta}_J d\Omega$$

$$\boldsymbol{K}^\rho_{IJ} = \boldsymbol{I} \int_\Omega N_I \frac{2\rho}{\Delta t} N_J d\Omega, \;\; M_{1s_{IJ}} = \int_\Omega \frac{1}{\kappa_s} N_I N_J d\Omega, \;\; \mathbf{Q}_{IJ} = \int_\Omega \mathbf{B}^T_I \mathbf{m} N_J d\Omega$$

$$M_{1f_{IJ}} = \int_\Omega \frac{1}{\kappa_f} N_I N_J d\Omega, \;\; M_{2f_{IJ}} = \int_\Omega \tau \frac{\rho}{\kappa_f} N_I N_J d\Omega, \;\; \tau = \left(\frac{8\tilde{\mu}}{h^2} + \frac{2\rho}{\delta} \right)^{-1}$$

$$M_{bf_{IJ}} = \int_{\Gamma_t} \frac{2\tau}{h_n} N_I N_J d\Gamma, \;\; L_{f_{IJ}} = \int_\Omega \tau (\boldsymbol{\nabla}^T N_I) \boldsymbol{\nabla} N_J d\Omega$$

$$f_{pf_I} = \int_{\Gamma_t} \tau N_I \left[\rho \frac{Dv_n}{Dt} - \frac{2}{h_n} (2\tilde{\mu} d_n - t_n) \right] d\Gamma - \int_\Omega \tau \boldsymbol{\nabla}^T N_I \boldsymbol{b} d\Omega$$

where N_I are the linear shape functions and h and δ are characteristic distances in space and time [52].

For 2D problems:

$$\boldsymbol{c}^\sigma_s = \begin{bmatrix} \kappa_s + \frac{4\mu}{3} & \kappa_s - \frac{2\mu}{3} & 0 \\ \kappa_s - \frac{2\mu}{3} & \kappa_s + \frac{4\mu}{3} & 0 \\ 0 & 0 & \mu \end{bmatrix}, \;\; \boldsymbol{c}^\sigma_f = \begin{bmatrix} \kappa_f + \frac{4\tilde{\mu}}{3\Delta t} & \kappa_f - \frac{2\tilde{\mu}}{3\Delta t} & 0 \\ \kappa_f - \frac{2\tilde{\mu}}{3\Delta t} & \kappa_f + \frac{4\tilde{\mu}}{3\Delta t} & 0 \\ 0 & 0 & \frac{\tilde{\mu}}{\Delta t} \end{bmatrix}$$

$$\boldsymbol{\beta}_I = \begin{bmatrix} \frac{\partial N_I}{\partial x} & \frac{\partial N_I}{\partial y} \end{bmatrix}^T, \;\; \mathbf{B}_I = \begin{bmatrix} \frac{\partial N_I}{\partial x} & 0 & \frac{\partial N_I}{\partial y} \\ 0 & \frac{\partial N_I}{\partial y} & \frac{\partial N_I}{\partial x} \end{bmatrix}^T, \;\; \mathbf{m} = [1, 1, 0]^T$$

Box 1. Matrices and vectors introduced in Algorithm 1 [26].

Consider a domain containing fluid and solid subdomains. The first step of the standard PFEM consists in the elimination of the previous distorted mesh. As in this work the PFEM is used for the fluid part only, at the beginning of a new calculation step (${}^n t$) only the fluid mesh is erased, while the solid is considered with the same mesh of the previous time step as shown in Figure 2a. Over this cloud of points, including the rigid and the boundary solid nodes, the new mesh is created using the Delaunay tessellation and the Alpha Shape method (Figure 2b). At this stage, it is possible to solve the governing equations to both fluid and solid subdomains with the FEM. The state variables are computed at the new configuration at ${}^n t + \Delta t$, according to the Updated Lagrangian description. After the FEM solution, the fluid mesh with the updated node positions is erased again (only the nodes are maintained) and the previous steps are repeated (Figure 2c).

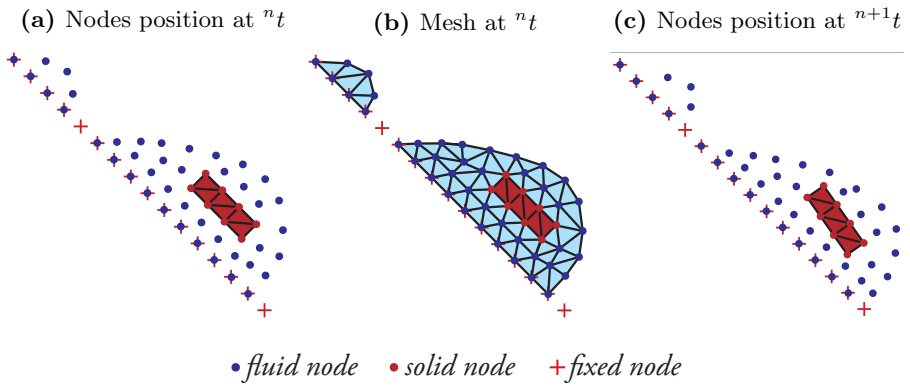

Figure 2: Sequence of PFEM remeshing. to update a "cloud" of fluid nodes and a discretized solid domain from time ${}^{n}t$ to time ${}^{n+1}t = {}^{n}t + \Delta t$.

4.1 Phase change modeling

A model for phase change is required in order to simulate numerically a nuclear meltdown scenario. In this approach, all the melting solid structures are transformed into the fluid material involved in the same analysis (*i.e.* the corium in the NSA simulations).

In this work, the phase change is studied only in terms of melting while the re-solidification is not modeled.

In the unified approach used here, both solids and fluids follow the same balance equations and adopt the same state variables. The only differences consist of the remeshing procedure, which is performed for the fluid domain only, and the specific constitutive laws.

Such similarity and compatibility between the fluid and the solid formulations are particularly helpful for modeling phase change phenomena.

In this approach, solid elements become part of the fluid domain when at least one of the following two criteria is satisfied:

1. *Temperature condition*. Phase change occurs if the mean temperature of the elements surrounding the same node is higher than the melting temperature of the material (Figure (3)).

2. *Condition on maximum plastic deformation*. A solid element becomes a fluid one if it has accumulated a plastic deformation larger than a maximum limit.

Both criteria refer to elemental quantities and they can coexist without coming into conflict. The temperature of each element is computed as the mean value of the nodal temperatures obtained from Eq.(6). This elemental mean temperature (plotted in the first picture of Figure (3)) is also used to update the temperature-dependent material parameters.

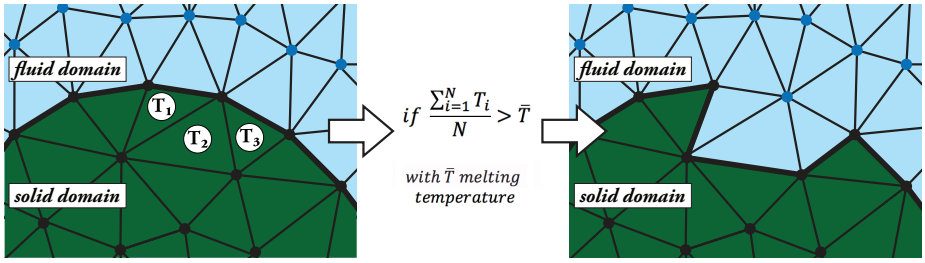

Figure 3: Graphic representation of the first criterion for phase change. The temperature plotted in the picture represents the mean temperature of the solid elements.

Note that those elements that are fulfilling the phase change criteria are more properly treated with the stabilized fluid PFEM than with the solid FEM hypoelasto-plastic model. In fact, the plastified zones behave as an incompressible material. Moreover, the large deformations suffered by these elements may deteriorate their geometrical quality, thus making necessary a local mesh regeneration.

Note also that the solid mesh just loses those elements that are transformed into fluid, while the same connectivity of the previous time step is kept in the rest of the domain. This means that the information of the elements at a solid state, stored at the respective Gauss points, is not lost and, therefore, interpolation procedures that may affect the method accuracy are not required either.

It is also important to analyze how much the phase change algorithm affects the convergence of the non-linear iterative loop. Phase change modeling induces an increasing non-linearity and may slow down the rate of convergence of the numerical scheme.

For the phase change algorithm above described, solid elements are transformed into fluid ones during the remeshing step, at the end of the non-linear iterations. However, these variations may still affect the convergence speed. In fact, at the beginning of the new step, fluid and solid configurations are different from the equilibrated ones obtained at the previous time step. These changes may slow down the convergence of the time step immediately after the transformation of some solid elements into fluid. However, the convergence speed is recovered quickly, typically in the following time step. In order to reduce the perturbation induced by these changes of topology, it is important to have a constitutive framework (as the one described in Sections 2.1 and 2.2) able to ensure a smooth transition from the solid to the fluid constitutive laws and material parameters.

An alternative to the proposed strategy is described in [7], where a PFEM formulation is used for tunneling simulation. In this approach, the solid boundary elements subject to excavation are progressively reduced and not erased during a unique time step. Specifically, the solid boundary nodes are moved inwards proportionally to the computed worn volume until the elements become smaller than a pre-arranged threshold and erased. This procedure may reduce

the perturbations induced by the phase change algorithm, but it requires an interpolation procedure over the solid boundary elements in order to update the elemental information in the new Gauss point positions.

5 Numerical examples and convergence check

The objective of this section is to analyze the convergence of the thermo-coupled FSI method here proposed. Two academic examples are considered. In the first one, the convergence rate of the temperature field as well as the time step dependency of the method are studied, while, the second example is used to verify the phase change convergence.

5.1 Heating of a rigid structure with a hot viscous fluid

A viscous fluid (μ=$15Pa \cdot s$) at $1000K$ is dropped over a rigid fixed structure at $500K$. The initial geometry of the 2D problem is shown in Figure 4.

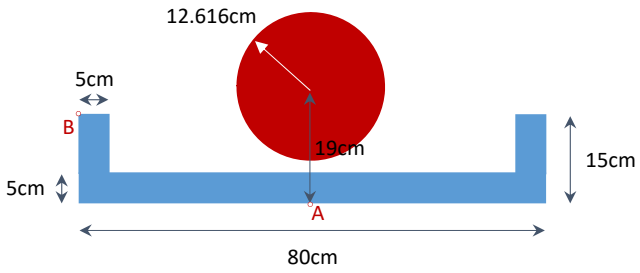

Figure 4: Heating of a rigid structure with a hot viscous fluid. Initial geometry.

The solid and fluid materials have the same density, $1000kg/m^3$, the same thermal properties, λ=$3000W/(m \cdot K)$ and c_v=$50J/(kg \cdot K)$, and the same surface, $50cm^2$. Under these conditions, fluid and solid should reach the equilibrium temperature of $750K$. A high value of heat conductivity has been used just for reducing the computational time of the analyses.

The problem has been studied for seven different meshes, spanning from the maximum mean mesh size of $15mm$ to the minimum one of $3mm$, with the aim of checking and analyzing the convergence of the scheme.

In Figure 5 the results obtained with the finest mesh are given. In order to highlight the progressive reaching of the equilibrium temperature, only a range of $30K$ around the equilibrium temperature is plotted over the fluid and solid bodies. If the temperature is out of this range, the limit color is plotted.

The convergence rate is analyzed in term of percentage error, computed as

$$error = \frac{v_{exp} - v_{fin}}{v_{exp}} \cdot 100 \tag{22}$$

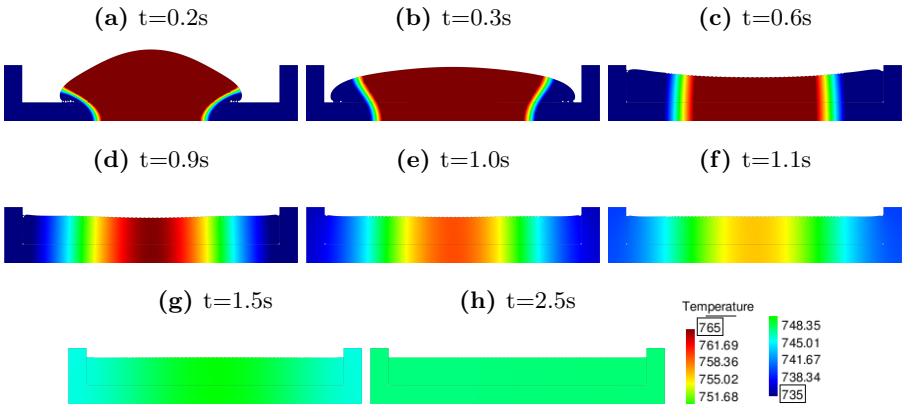

Figure 5: Heating of a rigid structure (initial temperature $500K$) with a hot viscous fluid (initial temperature $1000K$). Contours plotted for the temperature range $735K \leq T \leq 765K$.

where v_{exp} is the expected value and v_{fin} is the computed value at the end of the analysis when the equilibrium temperature is reached, namely at $t = 2s$. For the temperature field, $v_{exp} = 750K$. The same error measure has been used to quantify the error in terms of mass conservation induced by the PFEM solution. In this case the expected value is $50kg$ per unit of width.

As pointed out in Section 4, during the PFEM remeshing step some artificial changes of topology may occur and these may vary the global volume, hence also the mass of the computational domains [25]. In this particular case, as the fluid domain is getting close to the rigid structure, contact elements between the fluid and the solid boundaries are built, as shown in Figure 6. These elements increase

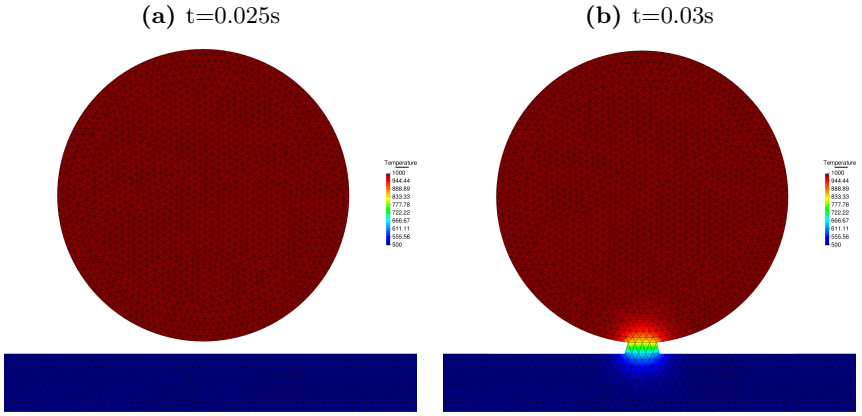

Figure 6: Creation of contact elements with the PFEM.

the fluid volume affecting the conservation properties of the scheme, and thus also the temperature solution accuracy. For this reason, the convergence of the

temperature field must be studied together with the mass conservation.

According to the percentage error measure of Eq.(22), a first order convergence is obtained for temperature and mass errors. This represents a further evidence of the direct relation between the conservation of mass, affected by the PFEM remeshing, and the energy balance. The convergence plots are shown in the graph of Figure 7.

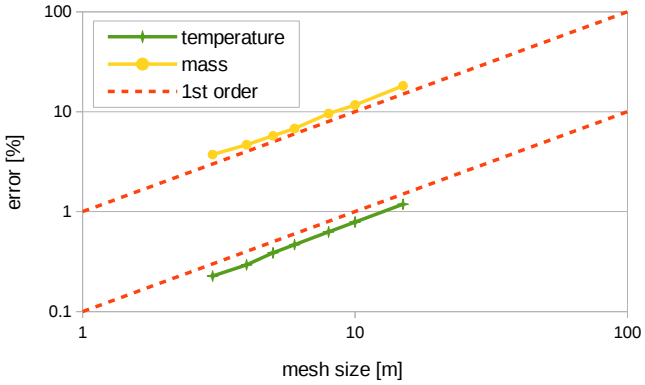

Figure 7: Heating of a rigid structure with a hot viscous fluid. Percentage error convergence for the equilibrium temperature and mass conservation.

The error reduces with mesh refinement and can be considered acceptable if reasonable fine meshes are used.

The same example has been used for analyzing the effect of the time step increment on the temperature field solution. For this purpose, the problem has been solved for an intermedium mesh using two different time steps, namely $10^{-3}s$ and $10^{-4}s$. This time step range is imposed by the mechanical problem, in particular is required to compute the first impact of the fluid against the solid. The temperature evolution at points A and B of Figure 4 is plotted in Figure 8.

The graphs show the temperature evolution at the mentioned points. The equilibrium temperatures are essentially the same for the two analyses, confirming that, for the range of time step interval suitable for the FSI solution, a weakly coupled fractional step scheme suffices for obtaining a reliable solution of the temperature field.

5.2 Melting of a solid beam

The efficiency of the phase change model is tested here for an academic 2D problem. The objective is to verify the implications of the phase change algorithm and to check if convergence with mesh refinement is ensured. The test case consists of a mass of hot viscous fluid (dynamic viscosity is $15Pa \cdot s$) that is dropped over a doubly clamped steel beam. In Figure 9 the initial geometry of the 2D problem is shown.

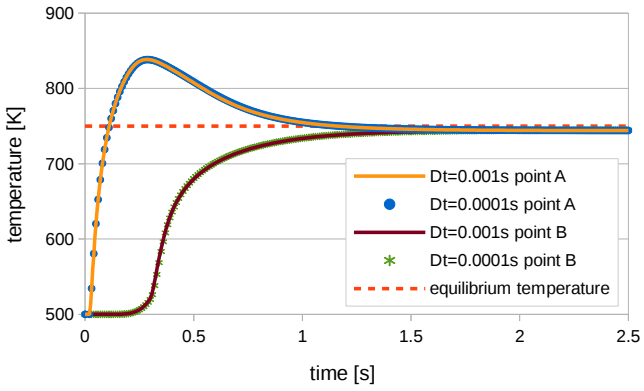

Figure 8: Heating of a rigid structure with a hot viscous fluid. Temperature evolution at points A and B of Figure 4 for the time increments $10^{-3}s$ and $10^{-4}s$, and expected equilibrium temperature.

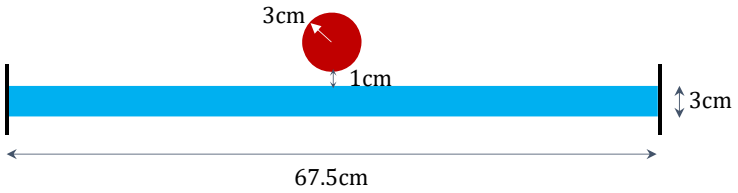

Figure 9: Melting of a solid beam. Initial geometry and data.

The initial temperatures of the fluid and the structure are $2000K$ and $360K$, respectively. As for the previous example, with the aim to reduce the computational time of the analyses, an extremely high heat conductivity ($2000W/(m{\cdot}K)$) is assumed for both fluid and solid, and a low melting point is considered for the structure, namely $700K$. Hence, the fluid can cool down but it cannot solidify. Fluid and solid densities are $7850Kg/m^3$.

Four instants of the simulation are plotted in Figure 10.

The viscous fluid heats up the central part of the beam, progressively creates a breach and finally flows down passing through the created hole. The snapshots show that the symmetry of the solution is adequately preserved.

In order to highlight the effect of the mesh size on the numerical scheme, the problem is studied for six different initial discretizations where mean mesh size h spans from $15mm$ (177 nodes) to $2mm$ (7032 nodes). The goal is to verify if the method, and in particular the phase change algorithm, is convergent and to detect for which mesh refinement the results can be considered reliable.

The amount of melted material produced at the end of each analysis ($t = 1s$) is the entity used to check convergence. In the graph of Figure 11 this value is given for the number of nodes used in the analyses. The graph shows

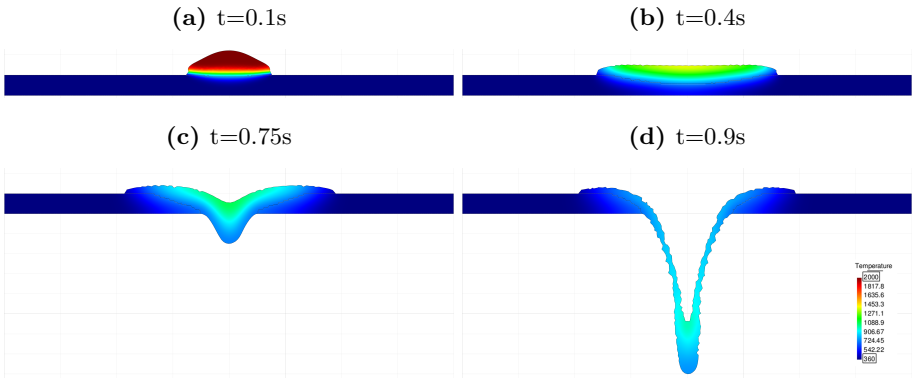

Figure 10: Melting of a beam induced by a volume of hot and viscous fluid.

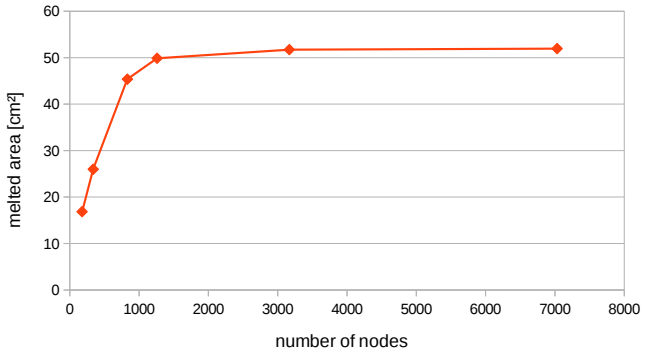

Figure 11: Amount of melted solid for six different meshes.

that there is a tendency for the melted area to increase with mesh refinement. However, from a mean mesh size of $5mm$ the amount of melted material keeps approximately constant.

This trend is also confirmed by the final configuration of the beam obtained for the different meshes, as plotted in Figure 12.

The results obtained with discretizations of a mean mesh size h lower than $6mm$ are very similar and the differences between the final configurations are negligible.

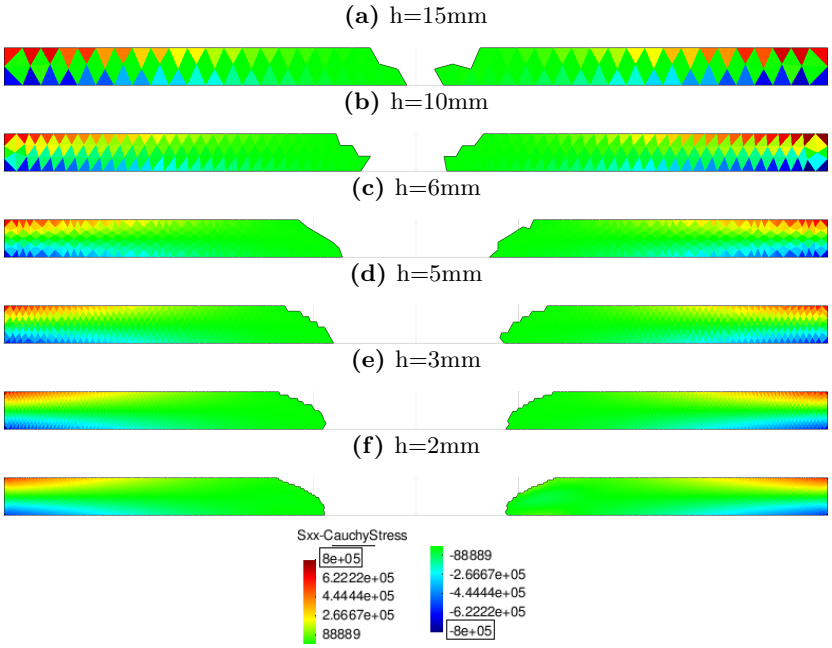

Figure 12: Residual solid structure at $t = 1.0s$ for six different discretizations. The x-component of the Cauchy stress tensor (σ_{xx}) is plotted over the finite element meshes.

6 Nuclear core melt accident scenario

This section is devoted to the numerical simulation of hypothetical scenarios of a nuclear core melt accident. The study is carried out for a Boiling Water Reactor (BWR), one of the most used nuclear reactors for the generation of electrical power. In Figure 13 a representation of the nuclear reactor and its main components is shown.

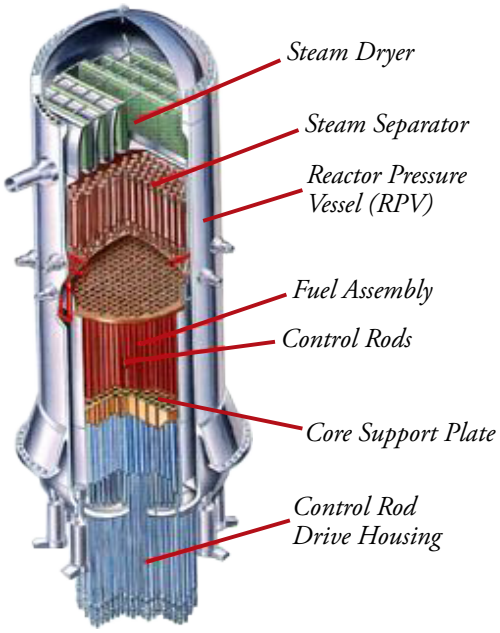

Figure 13: BWR vessel internals (picture adapted from [67]).

A core melt accident occurs when the heat generated by a nuclear reactor exceeds the heat removed by the cooling systems and at least one nuclear fuel element exceeds its melting point. The melted fuel dropping over the rest of the reactor components may induce their melting and the formation the corium. The last barrier of the nuclear reactor against the leakage of corium is represented by the reactor pressure vessel (RPV). Once this is breached, the corium can exit from the nuclear reactor contaminating the environment with its high level of radioactivity and toxicity.

In the accident occurred on March 2011 at the TEPCO's Fukushima Daiichi nuclear power plant station, a tsunami caused the stop of the emergency cooling system inducing an overheating within the RPV and the subsequent nuclear meltdown.

In the Fukushima disaster, due to the blackout, only small information could be recovered about the accident evolution and the amount of corium produced and its location are still unclear [58]. This lack of information about translates

into a high uncertainty about the definition of the Fukushima NSA. In this scenario, the role of numerical analysis for making NSA predictions therefore becomes of paramount importance.

In the next section, the hypotheses assumed in this work for the NSA models and their implications are discussed.

6.1 Model assumptions and implications

The high uncertainty around the nuclear meltdown makes it difficult to determine a reliable thermo-mechanical model for the corium as well as to define the right thermal conditions of the nuclear reactor during a NSA.

In such scenario, a more complicated model does not ensure necessarily a more realistic simulation of the NSA.

This section is entirely devoted to discuss the reasons and implications of the models used for predicting the mechanisms of a NSA studied in this work.

The corium has been modeled as a homogenous material according to the constitutive law presented in Section 2.1. However, being the corium a blend of nuclear reactor fuel and internal devices, a heterogeneous model may be more appropriate. In fact, generally, the fuel rods are composed by uranium dioxide (UO_2), the fuel cladding and the channel box are made of Zircaloy metals, while stainless steel is used for the core support plate, the fuel support piece and the control rods. All these materials are mixed in the corium mass with percentages that are highly affected by the core melt accident evolution.

In our work, the corium temperature has been kept constant and equal to the melting temperature of the fuel bars. This hypothesis is equivalent to use a very high thermal capacity for the corium or to assume a heat source due to the thermal reactions able to maintain its temperature constant.

Hence, neither the cooling of the corium nor its possible solidification are considered here, neither the chemical and radioactive reactions ($e.g$ the eutectic reaction between the zirconium (Zr) and the iron (Fe) contained in the stainless steel [32]).

Finally, in all the analyses the heat loss with the surrounding environment has been neglected.

Under these conditions, the hypothesis of keeping the corium temperature fixed and equal to the melting temperature of the fuel bars cannot be considered valid for simulations of large time intervals, because it would induce an excessive acceleration of the melting and failure of the solid structures.

However, this assumption can be considered acceptable for short time analyses that refer to the initial melting phase of the NSA, as the ones presented in the next section.

6.2 Models

Two hypothetical scenarios of the nuclear meltdown are studied.

The '*Plate model*' targets the simulation and analysis of the failure mechanism of the core support plate in contact with the melted fuel. The thermo-

plastic deformation, melting and collapse of the steel plate are studied considering an axisymmetric geometry. In the '*Clasp model*', melted fuel is progressively dropped within the fuel support clasp and the collapse of this 3D structure is reproduced.

The mechanical properties of all the solid components of the nuclear reactor involved in the analyses, as well as their temperature dependence, correspond to a standard stainless steel.

6.2.1 Plate model

The objective of this study is to analyze the damages induced by dropping melted fuel over the core support plate. The domain of interest includes the fuel assembly, the core support plate and the fuel support clasp, as shown in Figure 13. The fuel support clasp is modeled as a rigid body with a simplified

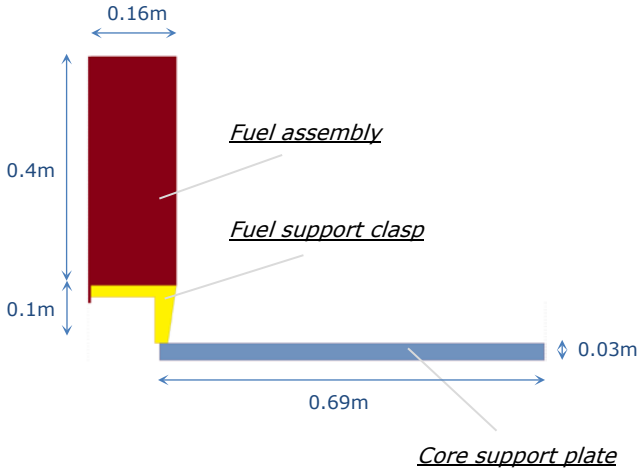

Figure 14: Global model. Initial geometry and finite element mesh.

geometry. In particular, the holes that allow the coolant supply have been neglected in order to facilitate the accumulation of melted fuel over the core support plate. A cylindrical shape has been considered for the fuel. Similarly, a cylindrical portion of the core support plate is considered. This allows for solving the problem using axisymmetric conditions.

The 2D domain has been discretized using a mesh of 3540 three-noded axisymmetric triangles and 2182 nodes.

The melting of the fuel assembly is achieved by progressively increasing the temperature of the fuel assembly up to its melting point ($T = 2000K$). The melted material is modeled as a Newtonian fluid with viscosity of $30Pa \cdot s$ dropping from its external side and falling over the core support plate (initially at $T = 360K$). In Figure 16 four snapshots of this initial phase are shown.

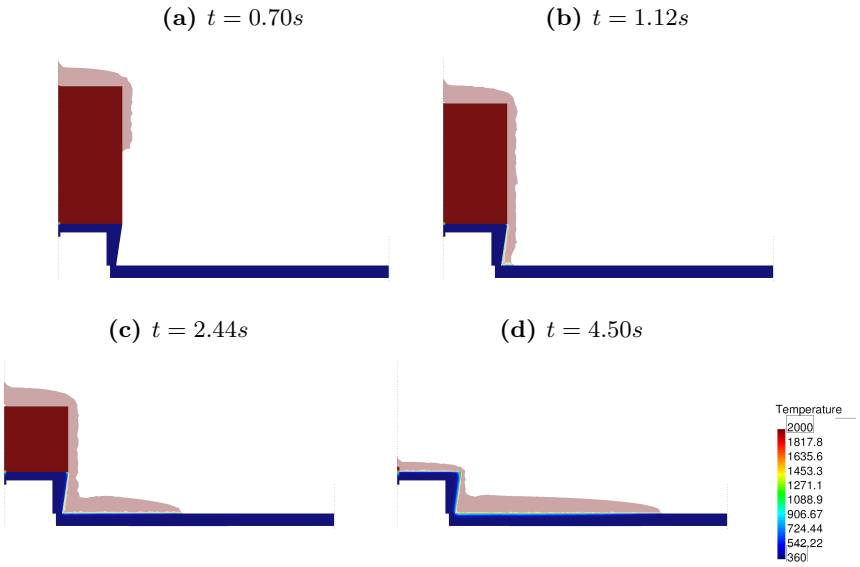

Figure 15: Plate model. Fuel assembly melting and dropping over the core support plate.

The interaction between the melted fuel and both the plate and the clasp induces their heating. The melting of the clasp is not allowed, while the melting temperature of the plate is fixed to $T = 1650K$. The plate phase change begins at around $t = 85s$ (Figure 15b) and its final failure occurs after $109s$ by high thermo-plastic deformations (Figures 16f-16h).

To better appreciate the failure mechanism of the plate, Figure 17 shows the deformed configuration of the solid structure with a magnification factor of 20. The contours of the pictures represent the mean temperature of the solid elements.

The pictures show the formation of a plastic mechanism. For $t = 109.00s$, the plate is still clamped at both ends, although most part of it has already melted (Figure 17c). However, after a while, the zone close to the inner side collapses after concentration of plastic strains (Figures 17d and 17e). At this stage, the plate is not fully clamped anymore and this produces an extra load over the external side of the plate (Figure 17f).

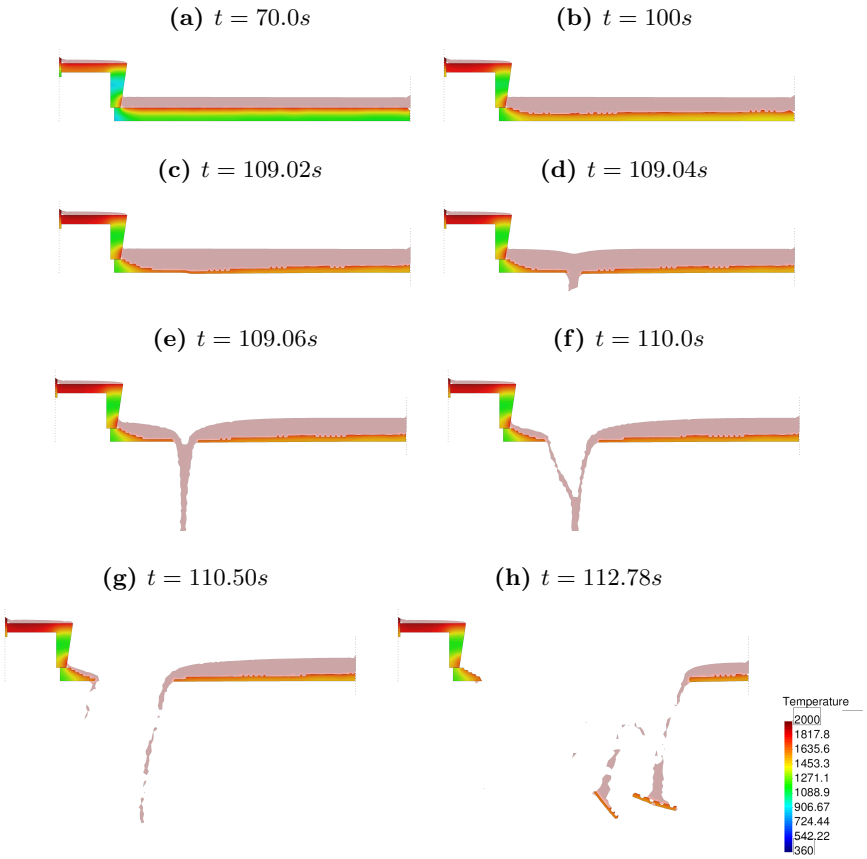

Figure 16: Plate model. Heating and failure of the core support plate.

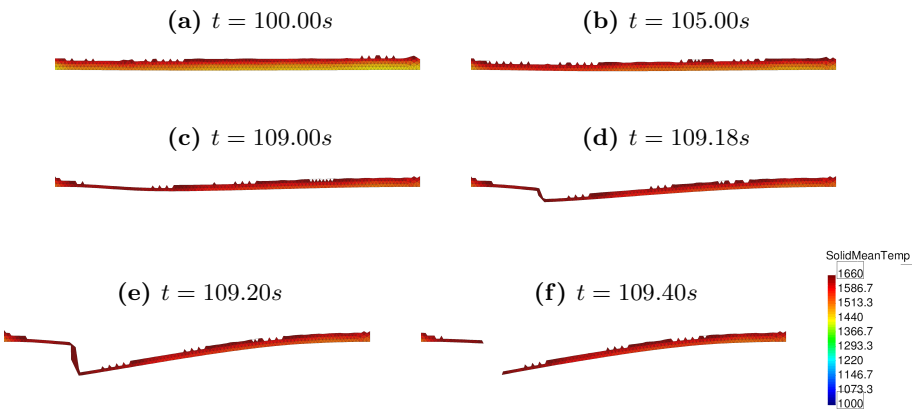

Figure 17: Plate model. Collapse of the core support plate (magnification factor 20).

6.2.2 Clasp model

The clasp represents the fuel support structure and is located within the holes of the core support plate, see Figure 13. The clasp is analyzed with a realistic geometry considering a cylindrical shape with four holes in its lateral walls. The clasp has a height of $55mm$ and its external surface has a radius of $40mm$. A volume of $52.73cm^3$ of melted fuel, initially modeled as a rigid and fixed body, is placed over the clasp and progressively falls down and penetrates into the structure. The temperature of the fuel is artificially increased from the bottom to the top. When the melting criteria are fulfilled, the rigid elements are transformed into fluid ones and computed according to the melted material model. The initial geometry of this model is given in Figure 18.

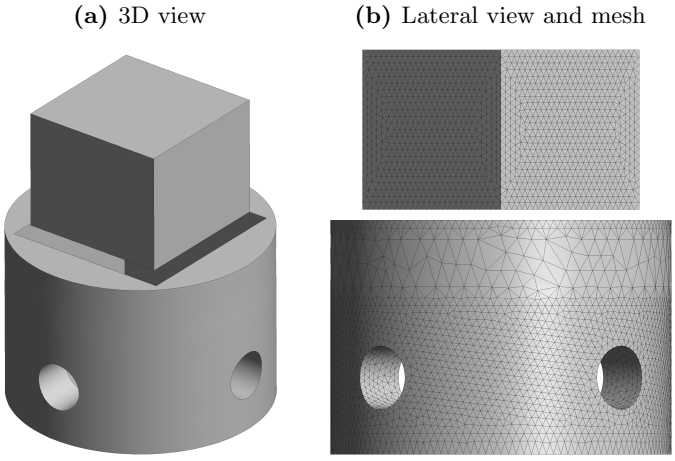

Figure 18: Clasp model. Initial geometry.

The upper part of the fuel support structure (where a coarser mesh is used) as well as the fuel assembly at solid state are considered as rigid and fixed.

The problem has been studied using an initial finite element mesh of 375427 4-noded tetrahedra and 75355 nodes using a mean mesh size of $4.75mm$ (Figure 18b).

The melted fuel, modeled as a viscous Newtonian fluid, falls down and accumulates in the inner part of the clasp. The contact with the fuel induces the heating of the clasp. The zones that heat up faster are the inferior surface of the clasp and the portions of walls between two consecutive lateral holes (Figures 19a- 19b). After $2.5s$ the melted fuel starts to flow away from the lateral openings while the bottom part of the clasp is approaching its melting point (Figures 19c and 19d). At around $t = 3.15s$, the bottom of the clasp collapses and the accumulated fuel falls away instantaneously (Figures 19e and 19f)

In Figure 20, the progressive increment of the effective von Mises stress induced by the fuel accumulation within the clasp and the melting of the clasp

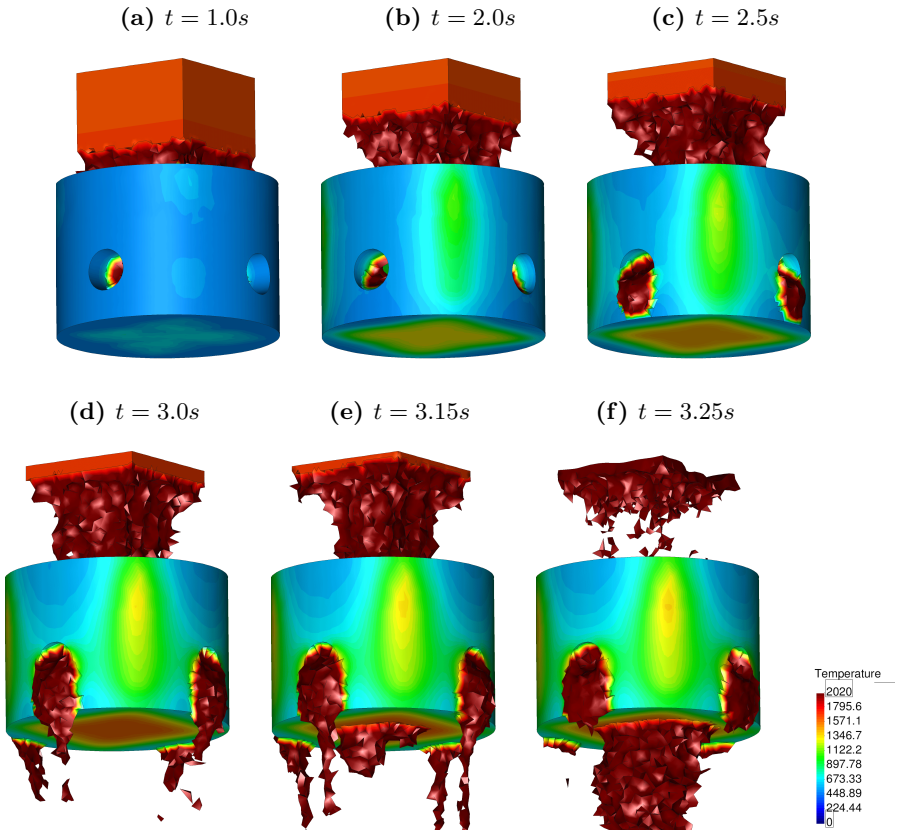

Figure 19: Clasp model. Melting of the fuel assembly and dropping of corium over the plate and the clasp.

structure is shown for three instants of the simulation.

Figure 21 shows four different views of the final configuration of the clasp with the corresponding temperature contours. The pictures show that the damages induced by the incandescent fuel affects the four lateral openings, as well as the bottom of the clasp where a huge hole is created.

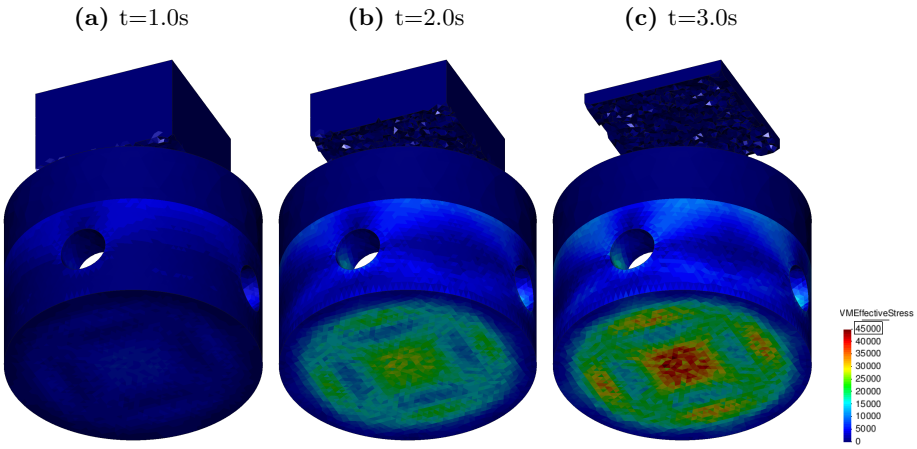

Figure 20: Von Mises effective stress plotted over the clasp structure.

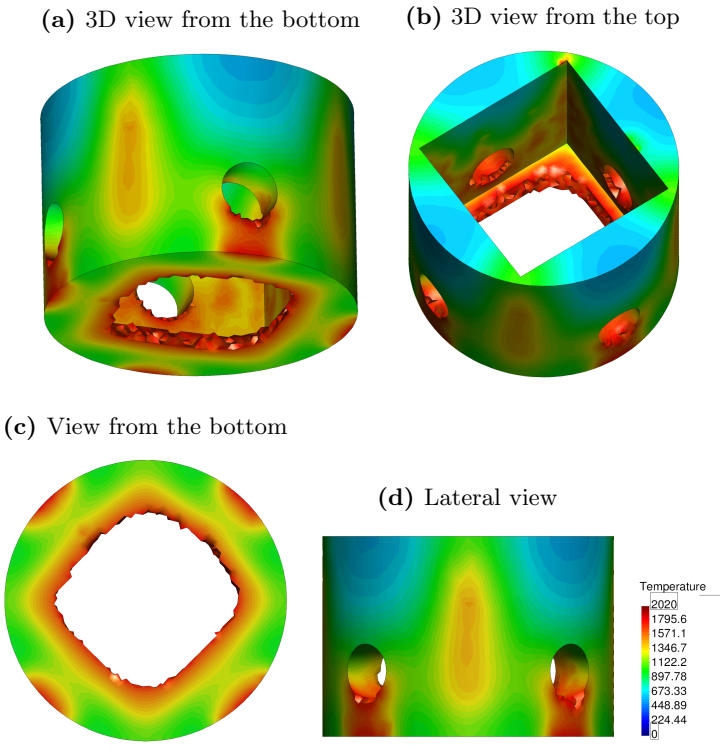

Figure 21: Clasp model. Final configuration of the clasp with the temperature field plotted.

7 Conclusions

In this work, A PFEM-based method for thermo-coupled FSI problems has been presented and its potential for simulating hypothetical scenarios of a nuclear core melt accident has been shown.

The method is derived from the so-called Unified formulation for FSI problems presented in [26]. In this work, the original numerical technique has been enhanced in order to account for the thermal effects and to model phase change phenomena.

The unified treatment of fluid and solid mechanics, together with the Lagrangian framework of the PFEM, has proven to be a suitable approach for modeling problems which involve large changes of topology and phase transformation.

The convergence of the thermo-coupled scheme and phase change algorithm has been demonstrated through the solution of two academic examples. The implications of the lack of mass preservation induced by the PFEM scheme, as well as the effect of the time step have been also analyzed and discussed. In particular, it has been shown that the temperature field accuracy is affected by the topological modifications induced by the PFEM remeshing while is not significantly altered by time increments variations within the range of time steps suitable for the mechanical problem solution.

The potential of the method for simulating the failure mechanisms induced by the corium in a nuclear meltdown scenario has been shown by reproducing two hypothetical NSA situations. In the first one, the melting and collapse of the core support plate induced by the melting fuel has been analyzed using an axisymmetric formulation, while, in the second analysis the breaching of the fuel support has been studied considering a 3D geometry. The simplifying hypotheses used in both simulations and their implications have also been discussed.

The numerical results have shown that the method is potentially able to handle the different phases of a NSA, from the melting of the fuel bars and the corium formation to its relocation within the pressure vessel and the collapse of the different structural components of the nuclear reactor.

8 Acknowledgments

This research was partially supported by the Japanese company Nippon Steeel and Sumitomo Metal Corporation (NSSMC). This support is gratefully acknowledged by the authors.

References

[1] F. Armero and J.C. Simo. A new unconditionally stable fractional step method for nonlinear coupled thermomechanical problems. *International Journal for Numerical Methods in Engineering*, 35:737–766, 1992.

[2] F. Armero and J.C. Simo. A priori stability estimates and unconditionally stable product algorithms for nonlinear coupled thermoplasticity. *International Journal of Plasticity*, 9:749–782, 1993.

[3] T. Belytschko, W.K. Liu, B. Moran, and K.I. Elkhodadry. *Nonlinear Finite Elements For Continua And Structures. Second Edition.* John Wiley & Sons, New York, 2014.

[4] T. Brepols, I. N. Vladimirov, and S. Reese. Numerical comparison of isotropic hypo- and hyperelastic-based plasticity models with application to industrial forming processes. *International Journal of Plasticity*, 63:18–48, 2014.

[5] F. Brezzi. On the existence, uniqueness and approximation of saddle-point problems arising from lagrange multipliers. *Revue française d'automatique, informatique, recherche opérationnelle. Série rouge. Analyse numérique*, 8(R-2):129–151, 1974.

[6] P. Bridgmain. *The Physics of High Pressure*. Bell & Sons, London, 1949.

[7] J.M. Carbonell, E. Oñate, and B. Suarez. Modelling of tunnelling processes and cutting tool wear with the particle finite element method (pfem). *Computational Mechanics*, 52 (3):607–629, 2013.

[8] M. Cervera, C. Agelet de Saracibar, and M. Chiumenti. Thermo-mechanical analysis of industrial solidification processes. *International Journal for Numerical Methods in Engineering*, 46:1575–1591, 1999.

[9] R. Chen, L. Chen, W. Tian, G. Su, and S. Qiu. Numerical analysis of the corium behavior within the fuel support piece by mps. *Proceedings of the 2016 24th International Conference on Nuclear Engineering*, 2016.

[10] R. Chen and Y. Oka. Numerical analysis of freezing controlled penetration behavior of the molten core debris in an instrument tube with mps. *Annals of Nuclear Energy*, 71:322–332, 2014.

[11] F.B. Cheung, S.W. Shiah, D.H. Cho, and M.J. Tan. Modeling of heat transfer in a horizontal heat-generating layer by an effective diffusivity approach. *ASME HTD 192*, pages 55–62, 1992.

[12] M. Chiumenti, M. Cervera, C. Agelet de Saracibar, and N Dialami. Numerical modeling of friction stir welding processes. *Computer methods in applied mechanics and engineering*, 254:353–369, 2013.

[13] M. Chiumenti, M. Cervera, N Dialami, B. Wu, L. Jinwei, and C. Agelet de Saracibar. Numerical modeling of the electron beam welding and its experimental validation. *Finite Elements in Analysis and Design*, 121:118–133, 2016.

[14] M. Chiumenti, M. Cervera, A. Salmi, C. Agelet de Saracibar, N Dialami, and K. Matsui. Finite element modeling of multi-pass welding and shaped metal deposition processes. *Computer Methods In Applied Mechanics And Engineering*, 199:2343–2359, 2010.

[15] M. Chiumenti, X. Lin, M. Cervera, W. Lei, Y. Zheng, and W. Huang. Numerical simulation and experimental calibration of additive manufacturing by blown powder technology. part i: thermal analysis. *Rapid Prototyping Journal*, 23(2):448–463, 2017.

[16] R. Codina, U. Schäfer, and E. Oñate. Mould filling simulation using finite elements. *International Journal of Numerical Methods for Heat & Fluid Flow*, 4(4):291–310, 1994.

[17] R. Codina and O. Soto. A numerical model to track two-fluid interfaces based on a stabilized finite element method and the level set technique. *International Journal for Numerical Methods in Fluids*, 40(1-2):293–301, 2002.

[18] M. Cremonesi, L. Ferrara, A. Frangi, and U. Perego. A lagrangian finite element approach for the simulation of water-waves induced by landslides. *Computer and Structures*, 89:1086–1093, 2011.

[19] C. Agelet de Saracibar, M. Cervera, and M. Chiumenti. On the formulation of coupled thermoplastic problems with phase-change. *International Journal of Plasticity*, 15:1–34, 1999.

[20] N. Dialami, M. Chiumenti, M. Cervera, and C. Agelet de Saracibar. Challenges in thermo-mechanical analysis of friction stir welding processes. *Archives of Computational Methods in Engineering*, 24:189–225, 2017.

[21] J.K. Dienes. On the analysis of rotation and stress rate in deforming bodies. *Computer Methods in Applied Mechanics and Engineering*, 32 (4):217–232, 1979.

[22] H. Edelsbrunner and E.P. Mucke. Three dimensional alpha shapes. *ACM Trans Graphics*, 13:43–72, 1999.

[23] H. Edelsbrunner and T.S. Tan. An upper bound for conforming delaunay triangulations. *Discrete and Computational Geometry*, 10 (2):197:213, 1993.

[24] M. Firat, K. Kaftanoglu, and B.Eser. Sheet metal forming analyses with an emphasis on the springback deformation. *Journal of Material Processing Technology*, 196 (1-3):135–148, 2008.

[25] A. Franci and M. Cremonesi. On the effect of standard pfem remeshing on volume conservation in free-surface fluid flow problems. *Computational Particle Mechanics*, pages 1–13, 2016.

[26] A. Franci, E. Oñate, and J. M. Carbonell. Unified lagrangian formulation for solid and fluid mechanics and fsi problems. *Computer Methods in Applied Mechanics and Engineering*, 298:520–547, 2016.

[27] A. Franci, E. Oñate, and J. M. Carbonell. Velocity-based formulations for standard and quasi-incompressible hypoelastic-plastic solids. *International Journal for Numerical Methods in Engineering*, 107 (11):970–990, 2016.

[28] G.Y. Goon, P.I. Poluchin, and B.A. Prudcowsky. The plastic deformation of metals. *Metallurgia*, Moscow, 1968.

[29] B. Haddag, T. Balan, and F. Abed-Meraim. Investigation of advanced strain-path dependent material models for sheet metal forming simulations. *International Journal of Plasticity*, 23 (6):951–979, 2008.

[30] C.W. Hirt and B.D. Nichols. Volume of fluid (vof) method for the dynamics of free boundaries. *Computational Physics*, 39:201–225, 1981.

[31] N.J. Hoff. Approximate analysis of structures in the presence of moderately large creep deformation. *Quarterly of Applied Mathematics*, 12 (1):49–55, 1954.

[32] P. Hofmann. Current knowledge on core degradation phenomena, a review. *Journal of Nuclear Materials*, 270:194–211, 1999.

[33] S.R. Idelsohn, N. Calvo, and E. Oñate. Polyhedrization of an arbitrary point set. *Computer Methods in Applied Mechanics and Engineering*, 92 (22–24):2649–2668, 2003.

[34] S.R. Idelsohn, J. Marti, A. Limache, and E. Oñate. Unified lagrangian formulation for elastic solids and incompressible fluids: Applications to fluid-structure interaction problems via the pfem. *Computer Methods In Applied Mechanics And Engineering*, 197:1762–1776, 2008.

[35] S.R. Idelsohn, E. Oñate, and F. Del Pin. The particle finite element method: a powerful tool to solve incompressible flows with free-surfaces and breaking waves. *International Journal for Numerical Methods in Engineering*, 61:964–989, 2004.

[36] S.R. Idelsohn, E. Oñate, F. Del Pin, and N. Calvo. Fluid-structure interaction using the particle finite element method. *Computer methods in applied mechanics and engineering*, 195:2100–2113, 2006.

[37] G. Johnson and D.J. Bammann. A discussion of the stress rate in finite deformation problems. *International Journal of Solids and Structures*, 20:725–737, 1984.

[38] J. Katsuyama, Y. Yamaguchi, Y. Kaji, and H. Yoshida. Development of failure evaluation method for bwr lower head in severe accident, 3; creep damage evaluation based on thermal-hydraulics and structural analyses. *Proceedings of the 2014 23rd International Conference on Nuclear Engineering*, 2014.

[39] A. Khan. *Continuum theory of plasticity*. John Wiley & Sons, New York, 1995.

[40] M. Kojić and K.J. Bathe. Studies of finite element procedures-stress solution of a closed elastic strain path with stretching and shearing using the updated lagrangian jaumann formulation. *Computers and Structures*, 26(1-2):175–179, 1987.

[41] S. Koshizuka and Y. Oka. Moving-particle semi-implicit method for fragmentation of incompressible fluid. *Nuclear science and engineering*, 123(3):421–434, 1996.

[42] Sandia National Laboratories. Melcor computer code manuals, vol. 1: Primer and users' guide, version 2.1.6840. *Sandia Report*, SAND 2015-6691, 2015.

[43] Sandia National Laboratories. Fukushima daiichi unit 1 accident progression uncertainty analysis and implications for decommissioning of fukushima reactors – volume i. *Sandia Report*, SAND 2016-0232, 2016.

[44] X. Li and Y. Oka. Numerical simulation of the surc-2 and surc-4 mcci experiments by mps method. *Annals of Nuclear Energy*, 73:46–52, 2014.

[45] L. Lubliner. *Plasticity theory*. Macmillan, New York, 1990.

[46] R.M. McMeeking and J.T. Rice. International journal of solids and structures. *Computer Methods In Applied Mechanics And Engineering*, 11 (5):601–616, 1975.

[47] K. Morita, S. Zhang, S. Koshizuka, Y. Tobita, H. Yamano, N. Shirakawa, F. Inoue, H. Yugo, M. Naitoh, H. Okada, Y. Yamamoto, M. Himi, E. Hirano, S. Shimizu, and M. Oue. Detailed analyses of key phenomena in core disruptive accidents of sodium-cooled fast reactors by the compass code. *Nuclear Engineering and Design*, 241 (12):951–963, 2011.

[48] T. Nagatake, H. Yoshida, K. Takase, and M. Kurata. Development of popcorn code for simulating melting behavior of fuel element; fundamental validation and simulation for melting behavior of simulated fuel rod. *Proceedings of the 2014 23rd International Conference on Nuclear Engineering*, 2014.

[49] J.C. Nagtegaal and J.E. De Jong. Some computational aspects of elastic-plastic large strain analysis. *Numerical Methods in Engineering*, 17 (1):15–41, 1981.

[50] J.C. Nagtegaal, D.M. Parks, and J.T. Rice. On numerical accurate finite elements solutions in the fully plastic range. *Computer Methods In Applied Mechanics And Engineering*, 4:153–177, 1974.

[51] F.H. Norton. The creep of steel at high temperatures. *McGraw-Hill*, New York, 1929.

[52] E. Oñate, A. Franci, and J.M. Carbonell. Lagrangian formulation for finite element analysis of quasi-incompressible fluids with reduced mass losses. *International Journal for Numerical Methods in Fluids*, 74 (10):699–731, 2014.

[53] E. Oñate, S.R. Idelsohn, F. Del Pin, and R. Aubry. The particle finite element method. an overview. *International Journal for Computational Methods*, 1:267–307, 2004.

[54] E. Oñate, J. Marti, R. Rossi, and S.R. Idelsohn. Analysis of the melting, burning and flame spread of polymers with the particle finite element method. *Computer Assisted Methods in Engineering and Science*, 20:165–184, 2013.

[55] W. Prager. *Introduction to Mechanics of Continua*. Ginn and Company, Boston, 1961.

[56] P. Ryzhakov, E. Oñate, and S.R. Idelsohn. Improving mass conservation in simulation of incompressible flows. *International Journal of Numerical Methods in Engineering*, 90:1435–1451, 2012.

[57] A. Saalfeld. In *Delaunay edge refinements*, pages 33–36, Burnaby, 1991.

[58] N. Sakai, H. Horie, H. Yanagisawa, T. Fujii, S. Mizokami, and K. Okamoto. Validation of maap model enhancement for fukushima dai-ichi accident analysis with phenomena identification and ranking table (pirt). *Journal of Nuclear Science and Technology*, 51 (7-8):951–963, 2014.

[59] N. Satoh, H. Ujita, k. Miyagi, N. Shirakawa, H. Horie, K. Nakahara, and H. Sasakawa. Development of molten core relocation analysis module mcra in the severe accident analysis code sampson. *Journal of Nuclear Science and Technology*, 37:225–236, 2000.

[60] J.C. Simo. On the computational significance of the intermediate configuration and hyperelastic stress relations in finite deformation elastoplasticity. *Mechanics of Materials*, 4 (3-4):439–451, 1985.

[61] J.C. Simo and T.J.R. Hughes. *Computational Inelasticity*. Springer, New York, 1998.

[62] J.C. Simo and M. Ortiz. A unified approach to finite deformation elastoplastic analysis based on the use of hyperelastic constitutive equations. *Computer Methods in Applied Mechanics and Engineering*, 49 (2):221–245, 1984.

[63] J.C. Simo and K.S. Pister. Remarks on rate constitutive equations for finite deformation problems: computational implications. *Computer Methods in Applied Mechanics and Engineering*, 46 (2):201–215, 1984.

[64] C. Truesdell. Hypo-elasticity. *Journal of Rational Mechanics and Analysis*, 4,1, 1955.

[65] H. Ujita, N. Satoh, M. Naitoh, M. Hikada, N. Shirakawa, and M. Yamagishi. Development of severe accident analysis code sampson in impact project. *Journal of Nuclear Science and Technology*, 36:11:1076–1088, 1999.

[66] MAAP webpage. http://www.fauske.com/nuclear/maap-modular-accident-analysis-program.

[67] Nuclear Street webpage. http://nuclearstreet.com/.

[68] PFEM webpage. www.cimne.com/pfem.

[69] A. Yamaji and X. Li. Development of mps method for analyzing melt spreading behavior and mcci in severe accidents. *Journal of Physics: Conference Series*, 739:012002, 2016.

[70] S. Yamashita, K. Takase, and H. Yoshida. Development of numerical simulation method for relocation behavior of molten materials in nuclear reactors: Analysis of relocation behavior for molten materials with a simulated decay heat model. *Proceedings of the 2014 23rd International Conference on Nuclear Engineering*, 2014.

[71] S. Yamashita, K. Tokushima, M. Kurata, K. Takase, and H. Yoshida. Development of numerical simulation method for melt relocation behavior in nuclear reactors: Validation of application for actual core support structures. *Proceedings of the 2016 24th International Conference on Nuclear Engineering*, 2016.

[72] M. Zhu and M. H. Scott. Modeling fluid-structure interaction by the particle finite element method in opensees. *Computers and Structures*, 132:12–21, 2014.

[73] O.C. Zienkiewicz and P.N. Godbole. Flow of plastic and visco-plastic solids with special reference to extrusion and forming processes. *International Journal for Numerical Methods in Engineering*, 8:3–16, 1974.

[74] O.C. Zienkiewicz, P.C. Jain, and E. Oñate. Flow of solids during forming and extrusion: Some aspects of numerical solutions. *International Journal of Solids and Structures*, 14:15–38, 1978.

[75] O.C. Zienkiewicz, E. Oñate, and J.C. Heinrich. A general formulation for the coupled thermal flow of metals using finite elements. *International Journal for Numerical Methods in Engineering*, 17:1497–1514, 1981.

[76] O.C. Zienkiewicz and R.L. Taylor. *The Finite Element Method for Solid and Structural Mechanics, Volume 2 (6th Ed.)*. Elsiever Butterworth-Heinemann, Oxford, 2005.